agriculture

MDPI

Article

Inversion of Soil Moisture Content in Silage Corn Root Zones Based on UAV Remote Sensing

Qihong Da [1,2], Jixuan Yan [1,2,*], Guang Li [2,3], Zichen Guo [1,2], Haolin Li [4], Wenning Wang [1,2], Jie Li [1,2], Weiwei Ma [2,3], Xuchun Li [1,2] and Kejing Cheng [1,2]

[1] College of Water Conservancy and Hydropower Engineering, Gansu Agricultural University, No. 1 Yingmen Village, Anning District, Lanzhou 730070, China; daqh@st.gsau.edu.cn (Q.D.); guozichen1993@lzb.ac.cn (Z.G.); wangwn@gsau.edu.cn (W.W.); uplijie@126.com (J.L.); lixc@st.gsau.edu.cn (X.L.); chengkj@st.gsau.edu.cn (K.C.)
[2] State Key Laboratory of Crop Science in Arid Habitat Co-Constructed by Province and Ministry, Lanzhou 730070, China; lig@gsau.edu.cn (G.L.); maww@gsau.edu.cn (W.M.)
[3] College of Forestry, Gansu Agricultural University, Lanzhou 730070, China
[4] College of Environmental Science and Engineering, Beijing University of Technology, Beijing 100124, China; lihaolin@bjut.edu.cn
* Correspondence: yanjx@gsau.edu.cn; Tel./Fax: +86-093-1763-2066

Abstract: Accurately monitoring soil moisture content (SMC) in the field is crucial for achieving precision irrigation management. Currently, the development of UAV platforms provides a cost-effective method for large-scale SMC monitoring. This study investigates silage corn by employing UAV remote sensing technology to obtain multispectral imagery during the seedling, jointing, and tasseling stages. Field experimental data were integrated, and supervised classification was used to remove soil background and image shadows. Canopy reflectance was extracted using masking techniques, while Pearson correlation analysis was conducted to assess the linear relationship strength between spectral indices and SMC. Subsequently, convolutional neural networks (CNNs), back-propagation neural networks (BPNNs), and partial least squares regression (PLSR) models were constructed to evaluate the applicability of these models in monitoring SMC before and after removing the soil background and image shadows. The results indicated that: (1) After removing the soil background and image shadows, the inversion accuracy of SMC for CNN, BPNN, and PLSR models improved at all growth stages. (2) Among the different inversion models, the accuracy from high to low was CNN, PLSR, BPNN. (3) From the perspective of different growth stages, the inversion accuracy from high to low was seedling stage, tasseling stage, jointing stage. The findings provide theoretical and technical support for UAV multispectral remote sensing inversion of SMC in silage corn root zones and offer validation for large-scale soil moisture monitoring using remote sensing.

Keywords: inversion of SMC; supervised classification; best variable combination; best result algorithm; best growth stage

Received: 24 December 2024
Revised: 24 January 2025
Accepted: 27 January 2025
Published: 2 February 2025

Citation: Da, Q.; Yan, J.; Li, G.; Guo, Z.; Li, H.; Wang, W.; Li, J.; Ma, W.; Li, X.; Cheng, K. Inversion of Soil Moisture Content in Silage Corn Root Zones Based on UAV Remote Sensing. *Agriculture* **2025**, *15*, 331. https://doi.org/10.3390/agriculture15030331

1. Introduction

As living standards continue to improve, individual domestic water consumption has increased significantly, exacerbating water resource shortages. Statistics show that agricultural water use accounts for 65% of the total water resources in China, yet its effective utilization rate is less than 45%, severely hindering the rapid development of agricultural production [1,2]. This issue is particularly acute in the arid regions of Northwest China, where scarce rainfall, high evaporation rates, and a dry climate frequently impair normal

crop growth, leading to reduced yields. Consequently, water scarcity has become a major factor restricting regional economic and social development [3]. Food security, as a cornerstone of national economic stability and people's livelihoods, fundamentally depends on water resources [4]. Addressing this challenge requires the development of precision agriculture to enhance water use efficiency [5]. Therefore, implementing the national food security strategy, establishing grain production bases, ensuring energy security, leveraging the resource advantages of the Hexi Corridor, promoting precision irrigation, and improving water resource utilization efficiency are critical foundations for building high-standard farmland and achieving sustainable agricultural development [6–8].

The Hexi region of Gansu Province, located in northwestern China, serves not only as a major production base for staple grains and cash crops but also as a critical area for exploring efficient water management strategies. Under conditions of scarce rainfall, arid climate, and high evaporation rates, the efficient utilization of water resources directly affects crop yields and the sustainability of agricultural production. Addressing the agricultural water challenges posed by water scarcity requires implementing precise irrigation during crop growth periods to maximize water use efficiency, which has become a central issue for agricultural development in this region [9]. Accurate inversion of SMC provides essential technical support for achieving this goal. However, with increasing population growth and the mounting pressure of climate change on water resource development, the region faces worsening imbalances between human activities and water resources, as well as environmental degradation [10]. Given the high water demands of silage maize, precision irrigation has become pivotal for ensuring crop growth and agricultural productivity. Consequently, UAV-based SMC inversion technology holds significant potential for application in the Hexi region.

In recent years, the use of remote sensing data for large-scale estimation of SMC has become a prominent research focus both domestically and internationally [11]. As a key indicator in agricultural monitoring, SMC plays a critical role in guiding precise irrigation decisions, evaluating crop growth conditions, and predicting yields [12]. Accurate and efficient assessment of SMC is essential for improving crop yield, quality, and agricultural water use efficiency [13]. Although traditional sampling methods provide precise measurements, they are time-consuming, labor-intensive, and limited in sample size, making them unsuitable for capturing SMC variations over large areas. Similarly, conventional SMC monitoring methods, such as the drying method, gamma-ray method, and neutron probe, cannot achieve real-time, non-contact, or non-destructive monitoring [14]. While traditional satellite remote sensing technologies have facilitated large-scale and rapid monitoring of soil moisture, their low temporal resolution and coarse spatial resolution often fail to meet the demands of precise irrigation [15,16]. Compared to traditional remote sensing technologies, unmanned aerial vehicle (UAV) technology has gained widespread attention due to its high spatial resolution, flexible flight planning, and real-time data acquisition capabilities [17]. These features overcome the limitations posed by satellite orbital cycles and adverse weather conditions. Unlike ground-based measurements, UAVs can cover large agricultural areas within a short time frame. The collected data, after appropriate processing, can serve as input for SMC model predictions, effectively replacing manual labor and enabling non-contact, non-destructive monitoring. Additionally, UAVs facilitate the transformation of sampling from point-based to area-based assessments, providing critical technological support for real-time SMC monitoring and precise irrigation in arid regions [18].

Currently, UAVs can be equipped with various sensors (e.g., RGB, multispectral, hyperspectral, and thermal infrared) to capture observational data with spectral, spatial, and temporal variations. These data are used for field surveys to assess crop water

stress [19–21], estimate crop nitrogen content [22–24], and monitor SMC [25–27]. For instance, Shafian et al. [28] estimated SMC over large agricultural areas by combining Landsat multispectral data with the perpendicular soil moisture index and DC data, achieving an R^2 of 0.703. However, this method is limited by Landsat's spatial resolution of 30 m, which is insufficient for small-scale precision irrigation in fields. In contrast, Liu et al. [29] employed a UAV equipped with a hyperspectral sensor to capture high-resolution images at the centimeter level, using a stacked ensemble learning model-DO to achieve SMC inversion with an R^2 of 0.81 and an RMSE of 1.6%. However, hyperspectral sensors are costly, and their data processing is complex, making them unsuitable for large-scale applications. Additionally, Qin et al. [30] proposed a method based on thermal infrared data combined with time-series analysis to monitor crop water stress. However, thermal infrared sensors are highly sensitive to weather conditions, which compromises their timeliness. UAVs equipped with multispectral sensors can estimate SMC by capturing the canopy reflectance and vegetation index (VI) [31,32]. Nevertheless, due to the three-dimensional structure of crops, images often contain shadows when the sensor's observation direction does not align with the sun's direct rays, which weakens the canopy spectral information and affects the accuracy of SMC inversion [33–35]. Given the limited number of multispectral bands, optimizing the band combination to improve inversion accuracy remains a challenge. This study addresses this gap by eliminating shadowed areas, optimizing band combinations, and exploring advanced algorithms such as neural networks and deep learning to enhance the robustness of SMC inversion models.

In summary, this study focuses on silage corn in Huarui Farm, Minle County, Zhangye City, Gansu Province, China. Using UAV multispectral imagery, we compare canopy reflectance before and after removing the soil background and image shadows, employ Pearson correlation analysis to select optimal spectral indices for different growth stages, and build SMC inversion models based on CNN, BPNN, and PLSR. The research objectives include: (1) comparing the accuracy of SMC inversion before and after removing the soil background and image shadows; (2) evaluating the spectral indices correlated with SMC; (3) assessing the effectiveness of CNN, BPNN, and PLSR models in inverting SMC; and (4) generating SMC inversion maps for the seedling, jointing, and tasseling stages.

2. Materials and Methods

2.1. Study Area

The experimental site for this study is located at Huarui Farm in Liuba Town, Minle County, Zhangye City, Gansu Province, China. (38°43′48.33″ N, 100°42′6.35″ E). It lies north of the Qilian Mountain watershed, in the middle section of the Hexi Corridor, and southeast of Zhangye City. The terrain slopes from south to north, with an elevation above 2400 m, and it has a temperate continental desert grassland climate. The main crops include corn, wheat, and potatoes. The soil in Minle County is grey-brown desert soil with a pH value of approximately 8.5. The organic matter content ranges from 0.2 to 2% in the plains and 0.8 to 10% in the mountainous areas. The average annual precipitation is 351 mm, with a frost-free period of 140 days. The experimental plot covers an area of about 3.5 mu (approximately 0.23 hectares), with silage corn planted at a spacing of 25 cm between plants and 50 cm between rows, using full plastic mulch coverage. The location of the study area is shown in Figure 1, and the field experiment layout is depicted in Figure 2.

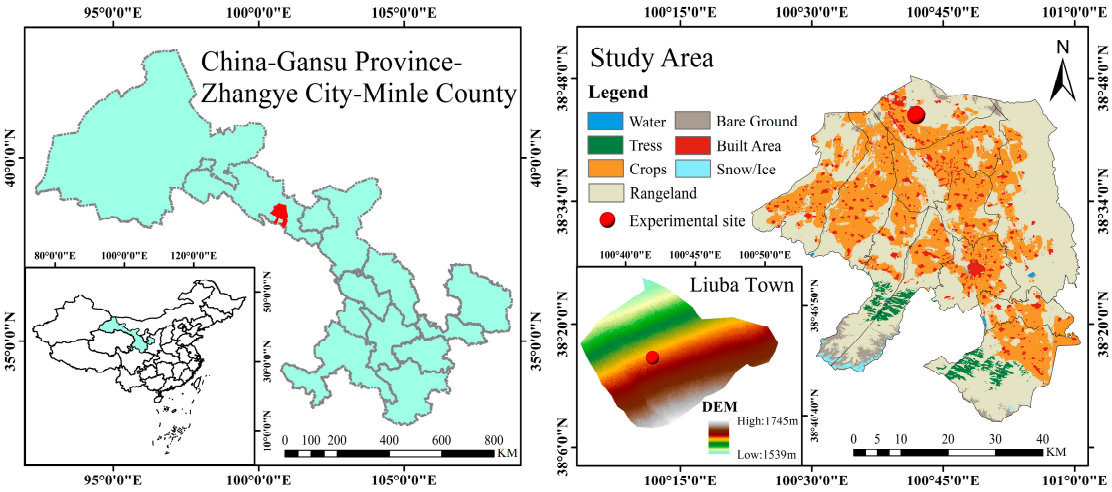

Figure 1. Overview of the study area. Note: On the left side is the research location map of Minle County, Zhangye City, Gansu Province, China. On the right is the land cover type of Minle County and the DEM of Liuba Town.

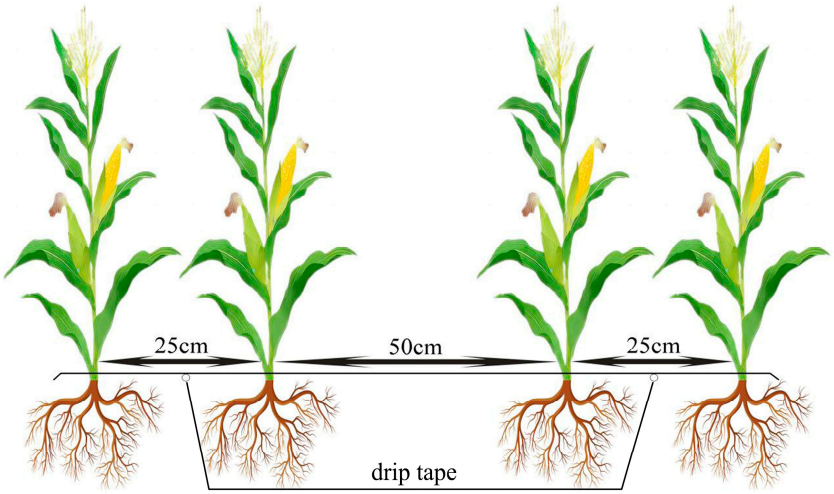

Figure 2. Field experiment layout. Note: The silage corn was planted with a spacing of 25 cm between plants and 50 cm between rows.

2.2. Data Acquisition

2.2.1. Spectral Image Acquisition and Processing

In this experiment, multispectral remote sensing images were acquired using a DJI Matrice 300 RTK quadcopter UAV (Shenzhen DJI Innovation Technology Co., Ltd., Shenzhen, China) on 18 May 2022, 1 July 2022, and 4 August 2022. The UAV was equipped with an MS600Pro multispectral camera (Changguang Yuchen Information Technology and Equipment (Qingdao) Co., Ltd., Qingdao, China). The flight altitude was set at 30 m, with a forward overlap rate of 80% and a side lap rate of 70%. The flights were conducted between 12:00 and 15:00, with the multispectral camera lens pointed vertically downward. Each flight followed a predetermined route, and the central wavelength reflectance of the diffuse reflectance panel is shown in Table 1. The flight speed was 7 m/s, and images of the calibration panel were taken on the ground before and after each flight. These calibration panel images were used for reflectance calibration to compensate for changes in lighting conditions, ensuring data consistency. The ground resolution was 2 cm, and each flight lasted about 30 min. Four ground control points (GCPs) were established in the study area, and accurate co-ordinates were obtained using RTK. Pix4D Mapper4.8.0 software was

used to register and precisely correct the images based on manually marked control points. During image processing, illumination variation was normalized within the same growth stage, and data from different growth stages were processed using histogram matching. This process generated accurate crop reflectance information. After setting each parameter, a raster digital surface model (DSM), orthophoto, and reflectance map containing the reflectance of each band were produced, facilitating the extraction of silage corn canopy reflectance. The research flow chart is shown in Figure 3.

Table 1. The central wavelength and reflectivity of the diffuse reflector.

Spectral Band	Center Wavelength /nm	Reflectance of Diffuse Reflector /%	Spectral Band	Center Wavelength /nm	Reflectance of Diffuse Reflector /%
Blue	450	60	Rededge 1	720	60
Green	555	60	Rededge 2	750	60
Red	660	60	NIR	840	60

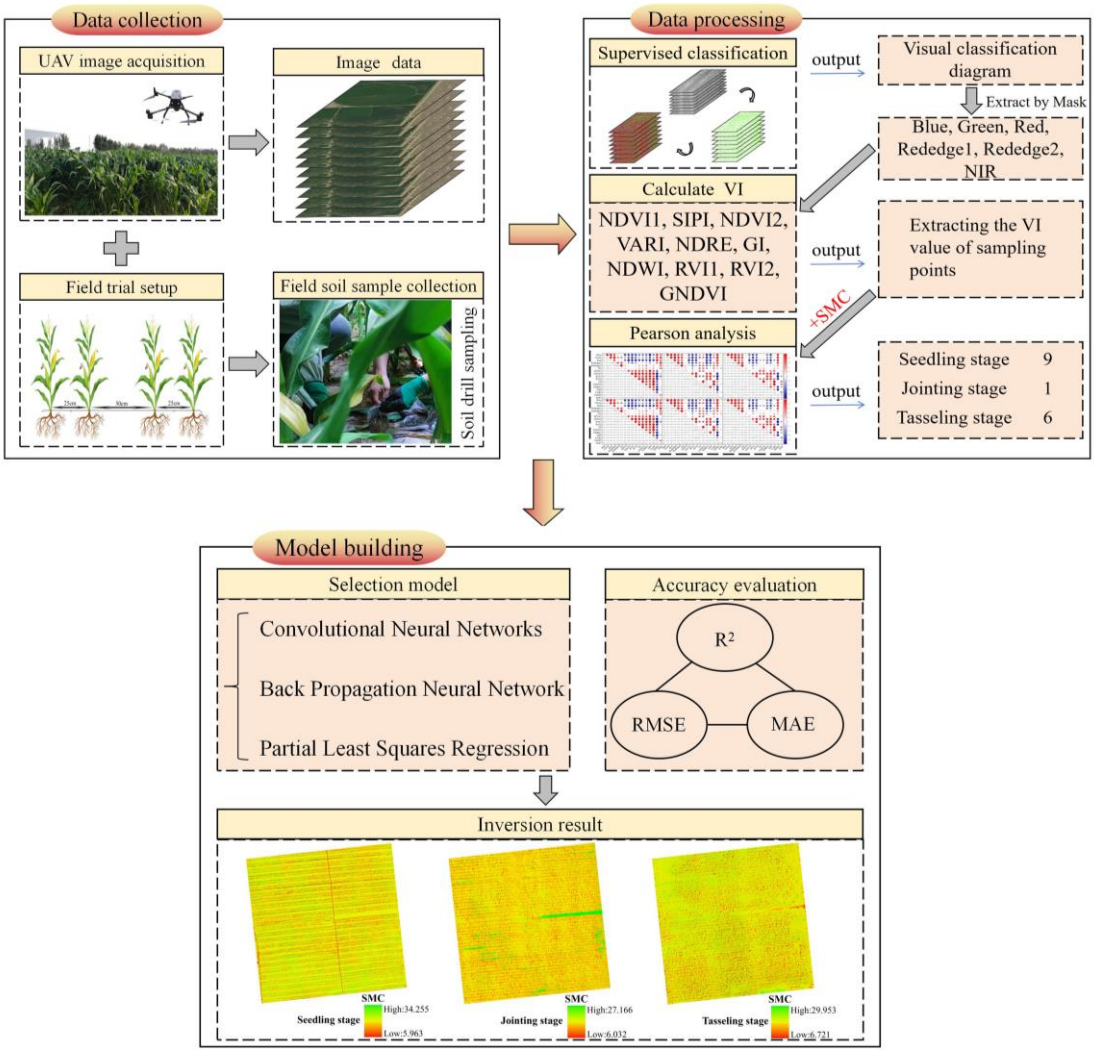

Figure 3. Overall flow chart of this study.

When acquiring images with the UAV, shadows caused by the misalignment of the solar direct radiation direction and the sensor observation direction can weaken the canopy spectral information. Therefore, false-color image combinations were used in the ENVI5.3 software for supervised classification. The maximum likelihood method, a widely used and

mature nonlinear classification based on the Bayesian criterion with minimal classification error probability, was used in this experiment to remove soil background and image shadows [36,37].

2.2.2. Soil Sample Collection and Processing

After UAV image acquisition, soil samples were promptly collected from the sampling points set according to Figure 4, and the SMC of the silage corn root zone was determined using the oven-drying method. Based on the depth of the primary root activity layer of silage corn, three depth levels were designed: 0–10 cm, 10–20 cm, and 20–30 cm. The average SMC across these depths was calculated as the SMC for each sampling point at 0–30 cm. Figure 5 shows the statistical results of the SMC sample data. The total number of soil moisture samples for the seedling, jointing, and tasseling stages was 48 for each stage. For each growth stage, 2/3 of the data was randomly selected for modeling, and the remaining 1/3 was used for validation. The specific dataset divisions are shown in Table 2.

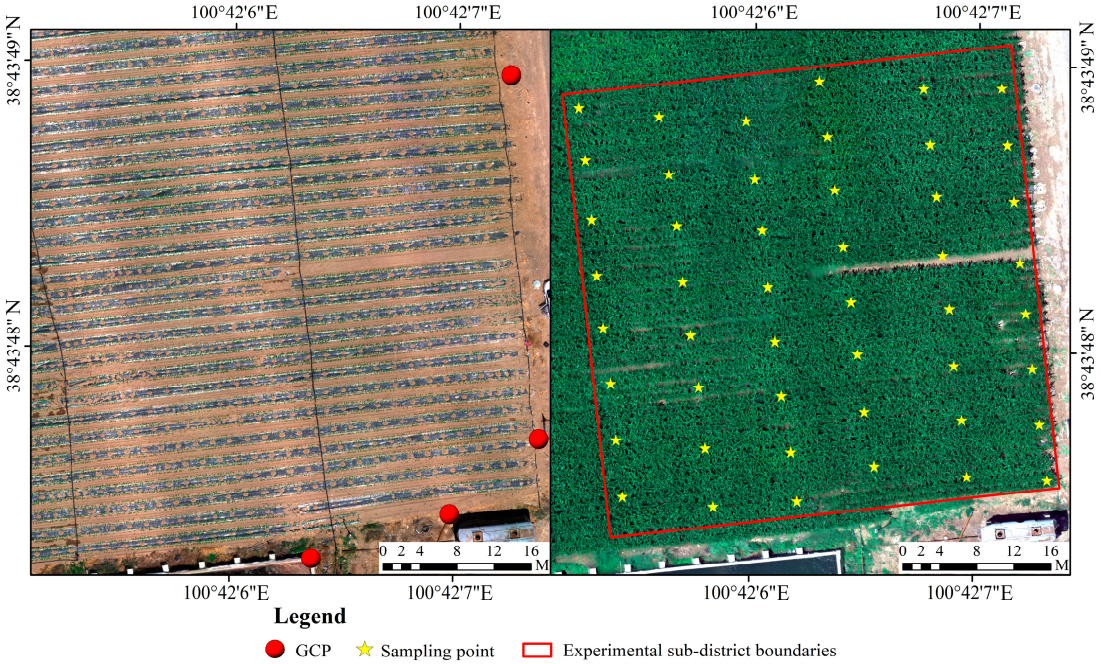

Figure 4. Sampling point layout. Note: Four ground control points (GCPs) were established within the study area, with sample points evenly distributed across the region. Precise coordinates were obtained using real-time kinematic (RTK) positioning. The UAV images were georeferenced and accurately corrected using Pix4D Mapper software by manually marking the control points.

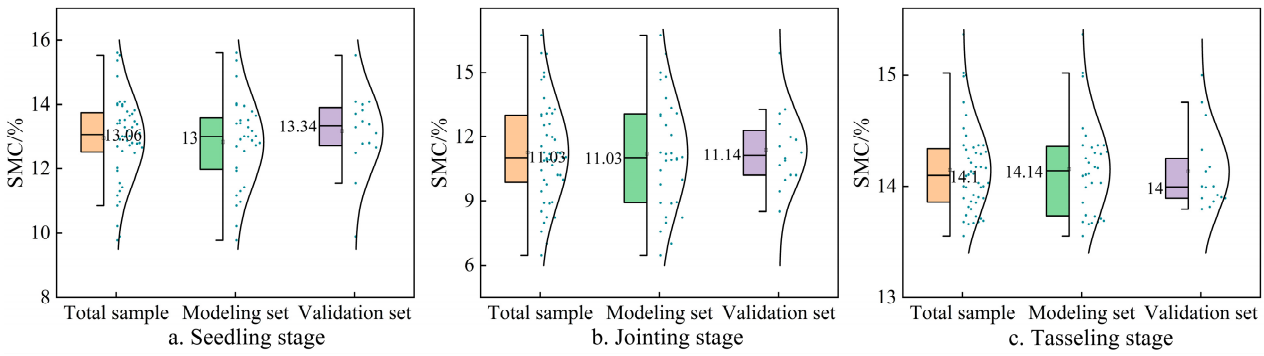

Figure 5. Statistics of SMC samples by fertility period. Note: (**a**–**c**) are the sample statistics of measured SMC at seedling stage, jointing stage, and tasseling stage, respectively, including the total sample set and the division of the modeling set and validation set.

Table 2. Statistics on datasets by fertility period.

Data Set	Seedling Stage	Jointing Stage	Tasseling Stage	Total
Modeling set	32	32	32	96
Validation set	16	16	16	48
Total	48	48	48	144

2.3. VI Extraction

The VI is a critical indicator for reflecting vegetation vitality and information. By analyzing the VI, we can effectively extract vegetation coverage, growth status, and trends [38]. In this study, we calculated 10 commonly used VIs based on corn canopy reflectance. The VIs and their calculation formulas are shown in Table 3.

Table 3. Vegetation index and calculation formulas.

Vegetation Index	Formulas	References
Normalized difference vegetation index 1	NDVI1 = (G − B)/(G + B)	[39]
Normalized difference vegetation index 2	NDVI2 = (NIR − R)/(NIR + R)	[40]
Normalized difference rededge index	NDRE = (NIR − RE1)/(NIR + RE1)	[41]
Green index	GI = G/R	[42]
Normalized green difference vegetation index	GNDVI = (G − R)/(G + R)	[43]
Structure intensive pigment index	SIPI = (NIR − B)/(NIR + B)	[44]
Ratio vegetation index 1	RVI1 = NIR/G	[45]
Ratio vegetation index 2	RVI2 = NIR/R	[46]
Visible atmospheric resistant index	VARI = (G − R)/(G + R − B)	[47]
Normalized differential water index	NDWI = (G − NIR)/(G + NIR)	[48]

Note: B, G, R, RE1, RE2, and NIR represent the spectral reflectance at wavelengths of 450, 555, 660, 720, 750, and 840 nm, respectively.

2.4. Pearson Correlation Analysis

Multispectral image data are characterized by complex combinations, and redundant and interfering spectral variables can affect the accuracy and precision of soil moisture inversion models. Therefore, it is necessary to select sensitive spectral index combinations [49]. This study primarily uses Pearson correlation analysis to evaluate the strength of the linear relationship between spectral indices and soil moisture content, which can be calculated using Equation (1), where X_i and Y_i represent sample values, and $\overline{X}$ and $\overline{Y}$ represent the sample mean values of the two, respectively:

$$r = \frac{\sum_{i=1}^{n} (X_i - \overline{X})(Y_i - \overline{Y})}{\sqrt{\sum_{i=1}^{n} (X_i - \overline{X})^2} \sqrt{\sum_{i=1}^{n} (Y_i - \overline{Y})^2}} \quad (1)$$

Note: The value range of r is $[-1, 1]$. Values of 0.8–1.0 indicate very strong correlation, 0.6–0.8 indicate strong correlation, 0.4–0.6 indicate moderate correlation, 0.2–0.4 indicate weak correlation, and 0.0–0.2 indicate very weak or no correlation.

2.5. Construction of SMC Inversion Models

In recent years, deep learning has been widely applied in disaster monitoring and pattern recognition [50–53], demonstrating significant advantages. Convolutional neural networks (CNNs) are one of the representative algorithms of deep learning, known for their local connections and weight sharing. CNNs excel in handling images, especially in image recognition tasks such as image classification, object detection, and image segmentation, making them one of the most widely used models.

The back propagation neural network (BPNN) is a multi-layer feedforward neural network trained using the error backpropagation algorithm. It is widely used for classification, regression, and prediction tasks, offering advantages such as non-linear mapping, self-learning, self-adaptation, and strong generalization ability [54,55].

Partial least squares regression (PLSR) is particularly suitable for prediction, as it can handle both reflective and formative indicators. PLSR can perform multivariate linear regression analysis, simplify data structures, and conduct canonical correlation analysis. It is the most commonly used method for parameter estimation in structural equation models with latent variables, capable of eliminating multicollinearity among variables and improving model accuracy [56,57].

This study uses MATLAB2022a to construct SMC inversion models using CNN, BPNN, and PLSR. To ensure that both the modeling and validation sets represent the statistical characteristics of SMC, the average of soil samples at various depths was taken. From each growth stage, 32 samples were randomly selected as the modeling sample set, with the remaining soil samples serving as the validation sample set.

2.6. Model Accuracy Evaluation

This study employed the *Kappa* coefficient to assess the consistency between classification results and reference data, considering the possibility of random agreement. The calculation formula is provided in Equation (2):

$$Kappa = \frac{P_0 - P_e}{1 - P_e} \tag{2}$$

where P_0 represents the observed agreement between the predicted and reference classifications and P_e denotes the expected agreement due to chance. A Kappa value of 1 indicates perfect agreement, while a value of 0 suggests that the classification is no better than random guessing. Typically, Kappa values above 0.8 are considered excellent, while values between 0.6 and 0.8 indicate substantial agreement.

In this study, the accuracy of the SMC inversion models was evaluated using mean absolute error (MAE), root mean square error (RMSE), and the coefficient of determination (R^2). MAE represents the average of the absolute errors and effectively reflects the actual prediction error; the smaller the MAE, the higher the model accuracy. RMSE indicates how close the predicted values are to the actual values, with values closer to 0 showing better accuracy. R^2 represents the goodness of fit of the model, with values closer to 1 indicating better inversion performance. The calculation formulas are shown in Equations (3)–(5):

$$R^2 = 1 - \frac{\sum_{i=1}^{n} (y_i - \hat{y}_i)^2}{\sum_{i=1}^{n} (y_i - \overline{y})^2} \tag{3}$$

$$RMSE = \sqrt{\frac{\sum_{i=1}^{n} (\hat{y}_i - y_i)^2}{\mathrm{n}}} \tag{4}$$

$$MAE = \frac{1}{n} \sum_{i=1}^{n} |\hat{y}_i - y_i| \tag{5}$$

where y_i is the measured value of soil moisture content, $\hat{y}_i$ is the predicted value of soil moisture content, $\overline{y}$ is the average value of soil moisture content, and n is the number of samples.

3. Results

3.1. Extraction and Statistical Analysis of Canopy Spectral Reflectance

This study processed the results of UAV multispectral images under supervised classification to obtain canopy vector files for silage corn. The Kappa coefficient reflects the accuracy of the classifier, and the evaluation of the classification results is shown in Table 4. The overall accuracy of the supervised classification reached 99%, with Kappa coefficients consistently above 0.99, which is beneficial for subsequent SMC inversion. Among all growth stages, the supervised classification performed best during the seedling stage of silage corn. The extraction process of silage corn canopy reflectance is illustrated in Figure 6.

Table 4. Classification accuracy and Kappa coefficient.

Growth Stages	Accuracy/%	Kappa Coefficient
Seedling stage	99.91	0.9986
Jointing stage	99.57	0.9952
Tasseling stage	99.69	0.9964

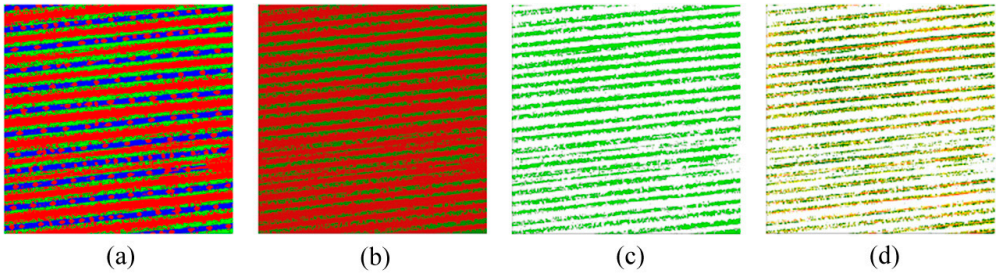

Figure 6. Extraction process of maize canopy reflectance. (**a**) Classification result. (**b**) Plant bands were extracted. (**c**) Canopy vector files were constructed. (**d**) Canopy reflectance was extracted.

The average spectral data for each growth stage were calculated to compare the changes in canopy reflectance of silage corn before and after the removal of the soil background and image shadows. The results are shown in Figure 7. Among the different growth stages, the near-infrared band of the canopy spectral reflectance shows the most significant increase after the removal of the soil background and image shadows. The seedling stage exhibits a greater increase in canopy spectral reflectance compared to the jointing and tasseling stages.

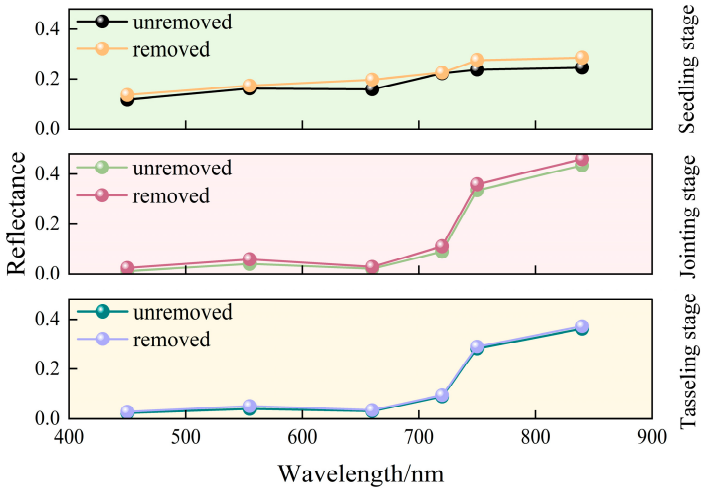

Figure 7. Spectral reflectance of maize canopy at different growth stages.

3.2. Pearson Correlation Analysis to Screen the Best Combination of Variables

To mitigate potential overfitting in the inversion model, Pearson correlation coefficients were employed to conduct multivariate correlation analysis between the independent variables (multi-spectral remote sensing data and spectral information) and the dependent variable (SMC in the root zone of silage corn) [58]. Figure 8 shows the scatter plot matrix and Pearson correlation coefficients for each growth stage after removing the soil background and image shadows, displaying the results of normality tests on the data. The diagonal of the matrix plots shows univariate density estimates, representing the distribution of each feature, while the other parts of the scatter matrix depict linear relationships between different variables.

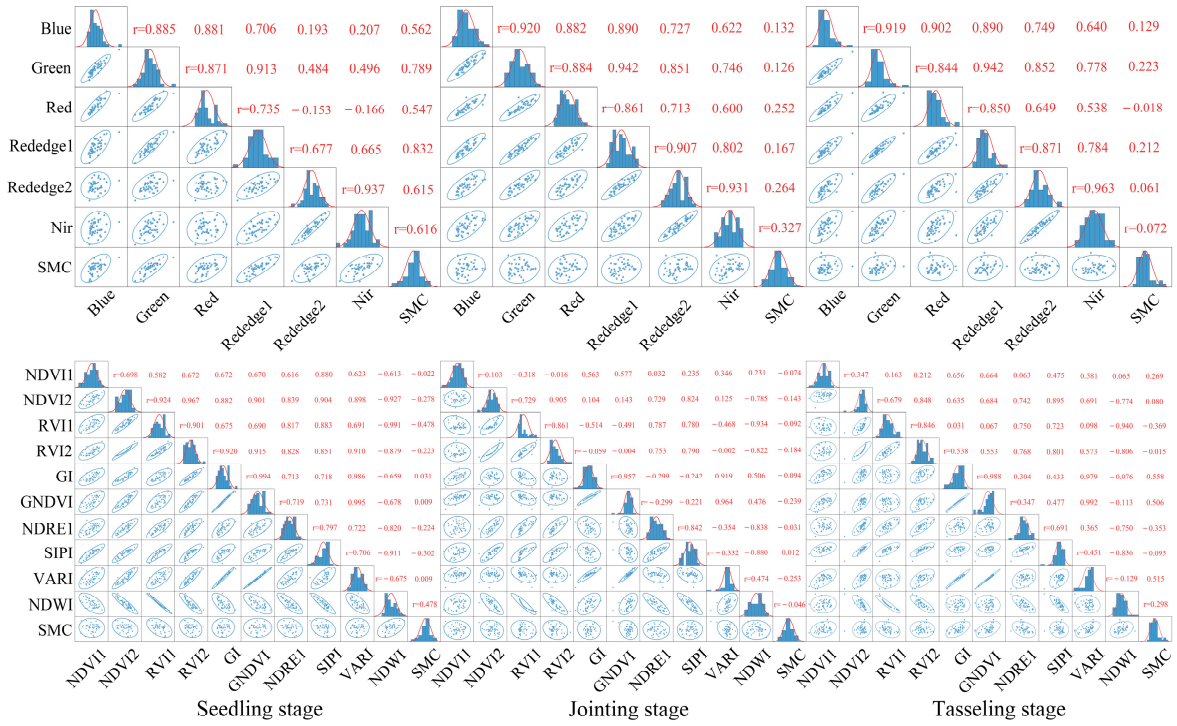

Figure 8. Scatter matrix and Pearson correlation analysis. The lower triangular matrix represents the linear relationship between spectral indices and SMC after removing the soil background and image shadows. The upper triangular matrix shows the correlation coefficients between variables.

Using Pearson correlation analysis, the optimal variable combinations for different growth stages were selected before and after removing the soil background and image shadows. After removal, the spectral indices most strongly correlated with SMC during the seedling stage, in order of strength, are Rededge1, Green, NIR, Rededge2, Blue, Red, NDWI, RVI1, and NDVI2, with correlation coefficients of 0.832, 0.789, and 0.616 for Rededge1, Green, and NIR, respectively. In the jointing stage, NIR showed the highest correlation with SMC, with a coefficient of 0.327. In the tasseling stage, the indices GI, VARI, and GNDVI exhibited higher correlations with SMC, with coefficients of 0.558, 0.515, and 0.506, respectively. During the tasseling stage, NDVI2 showed little to no correlation with SMC, suggesting a nonlinear relationship or no significant association between them. The statistical results of Pearson correlation analysis for selecting the optimal variable combinations are summarized in Table 5.

Table 5. Pearson correlation analysis screening results statistics.

Treatment	Growth Stages	Number of Variables	Optimal Combination of Variables
unremoved	Seedling stage	9	Rededge1 ***, Green ***, Red ***, Rededge2 ***, NIR ***, Blue ***, NDWI ***, RVI1 ***, NDVI2 *
	Jointing stage	1	NIR *
	Tasseling stage	6	GI ***, VARI ***, GNDVI ***, RVI1 **, NDRE *, NDWI *
removed	Seedling stage	9	Rededge1 ***, Green ***, NIR ***, Rededge2 ***, Blue ***, Red ***, NDWI ***, RVI1 ***, SIPI *
	Jointing stage	1	NIR *
	Tasseling stage	6	GI ***, VARI ***, GNDVI ***, RVI1 **, NDRE *, NDWI *

Note: ***, **, * represent the significance level of 0.1%, 1%, and 5%, respectively.

3.3. Construction of SMC Inversion Model

The spectral indices highly correlated with SMC were selected to construct SMC inversion models based on CNN, BPNN, and PLSR. The CNN model utilized 2D convolutional layers and 2D pooling layers to process the data, which helps capture features in the 2D spatial domain. The convolution kernel size was [3, 1], and the pooling layer used a 2D max pooling layer with a pooling window size of [2, 1] and a stride of [1, 1]. The PLSR and BP models use 1D data for modeling and prediction, presenting multiple evaluation metrics to assess model performance. The BP model created two hidden layer neurons, with training parameters including 1000 iterations, an error threshold of 1e-6, and a learning rate of 0.01. Early stopping was implemented during the training process to prevent overfitting caused by excessive iterations. The SMC predictions obtained from inversion were linearly fitted to the SMC measurements obtained by the drying method, obtaining a fitting equation as shown in Figure 9, and analyzing the impact of the soil background and image shadows on the inversion model.

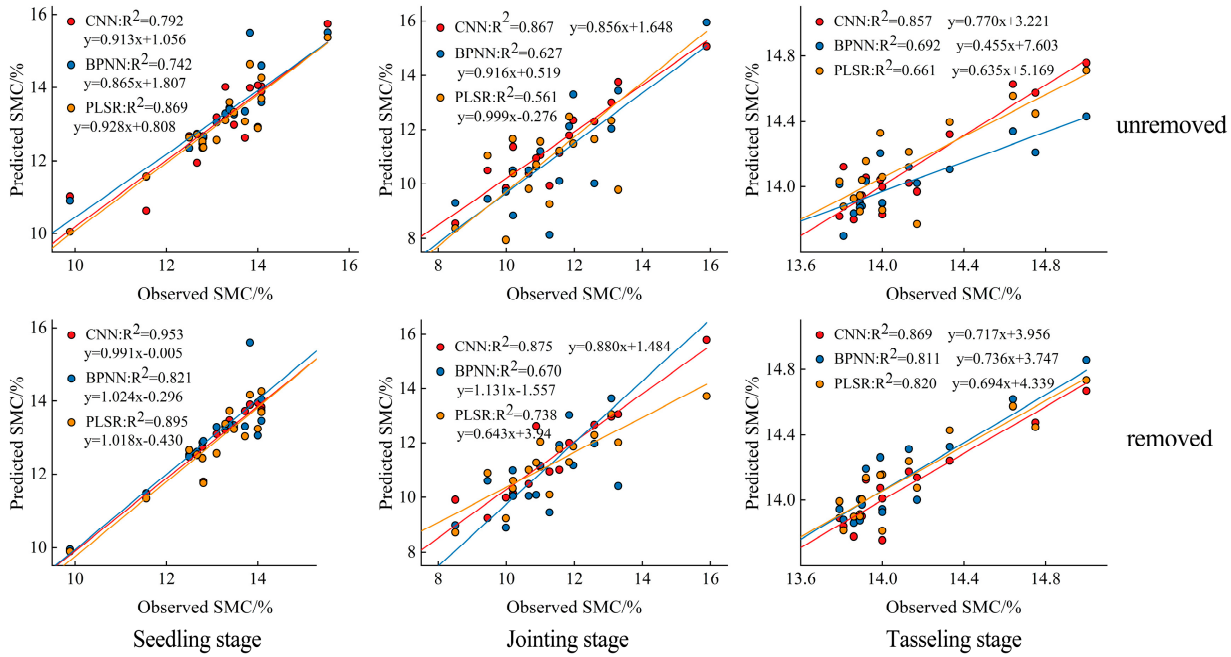

Figure 9. Inversion effect of soil moisture content (SMC).

As shown in Figure 9, removing the soil background and image shadows significantly enhances the retrieval accuracy of SMC. During the seedling stage, after removal, the R^2

values for CNN, BPNN, and PLSR increased by 0.161, 0.079, and 0.026, respectively. In the jointing stage, following removal, the R^2 values for CNN, BPNN, and PLSR improved by 0.008, 0.043, and 0.177, respectively. During the tasseling stage, after removal, the R^2 values for CNN, BPNN, and PLSR increased by 0.012, 0.119, and 0.159, respectively. Additionally, after background removal, CNN shows a decreasing trend in R^2 with the progression of growth stages, while BPNN and PLSR initially decrease and then increase in R^2. In summary, from the model perspective, the retrieval accuracy ranks as follows: CNN > PLSR > BPNN. From the growth stage perspective, the ranking is as follows: seedling stage > tasseling stage > jointing stage.

3.4. Comprehensive Evaluation of SMC Inversion Models

As shown in Table 6, this study evaluates the accuracy of three SMC inversion models before and after removing the soil background and image shadows from the perspectives of MAE, RMSE, and R^2. The analysis reveals the following: (1) After removing the soil background and image shadows, the accuracy of SMC inversion results improved for all growth stages across the three inversion models. CNN exhibited the highest accuracy, with validation set R^2 increasing by 20.33%, 0.92%, and 1.28% for each growth stage, MAE values of 0.156, 0.341, and 0.101, and RMSE values of 0.284, 0.595, and 0.143, respectively. For BPNN, validation set R^2 increased by 10.65%, 6.86%, and 17.20%, with MAE values of 0.315, 1.025, and 0.120, and RMSE values of 0.552, 1.308, and 0.154, respectively. PLSR showed an increase in validation set R^2 by 2.87%, 31.55%, and 24.05%, with MAE values of 0.357, 0.662, and 0.128, and RMSE values of 0.447, 0.882, and 0.155, respectively. (2) During the seedling stage, under conditions of removing the soil background and image shadows, the modeling set R^2 for CNN, BPNN, and PLSR was 0.960, 0.906, and 0.727, respectively. During the jointing stage under the same conditions, the modeling set R^2 was 0.875, 0.670, and 0.738, respectively, and during the tasseling stage, 0.869, 0.811, and 0.820, respectively. The model inversion accuracy for each growth stage ranks from highest to lowest as CNN, PLSR, and BPNN.

Table 6. Evaluation of model inversion results.

Model	Treatment	Growth stages	Modeling Set			Validation Set		
			MAE	RMSE	R^2	MAE	RMSE	R^2
CNN	unremoved	Seedling stage	0.223	0.320	0.948	0.412	0.555	0.792
		Jointing stage	0.522	0.911	0.883	0.438	0.602	0.867
		Tasseling stage	0.083	0.149	0.898	0.099	0.136	0.858
	removed	Seedling stage	0.161	0.278	0.960	0.156	0.284	0.953
		Jointing stage	0.556	0.87	0.893	0.341	0.595	0.875
		Tasseling stage	0.075	0.106	0.934	0.101	0.143	0.869
BPNN	unremoved	Seedling stage	0.494	0.660	0.761	0.389	0.608	0.742
		Jointing stage	1.164	1.465	0.675	0.836	1.233	0.627
		Tasseling stage	0.156	0.182	0.812	0.169	0.239	0.692
	removed	Seedling stage	0.297	0.453	0.906	0.315	0.552	0.821
		Jointing stage	1.199	1.476	0.682	1.025	1.308	0.670
		Tasseling stage	0.135	0.169	0.831	0.120	0.154	0.811
PLSR	unremoved	Seedling stage	0.607	0.764	0.697	0.339	0.447	0.870
		Jointing stage	1.415	1.719	0.681	1.118	1.449	0.561
		Tasseling stage	0.209	0.236	0.688	0.164	0.200	0.661
	removed	Seedling stage	0.579	0.718	0.727	0.357	0.447	0.895
		Jointing stage	1.272	1.487	0.785	0.662	0.882	0.738
		Tasseling stage	0.187	0.216	0.726	0.128	0.155	0.820

According to the comprehensive evaluation results of the prediction model, the SMC inversion results for the experimental area are presented in Figure 10.

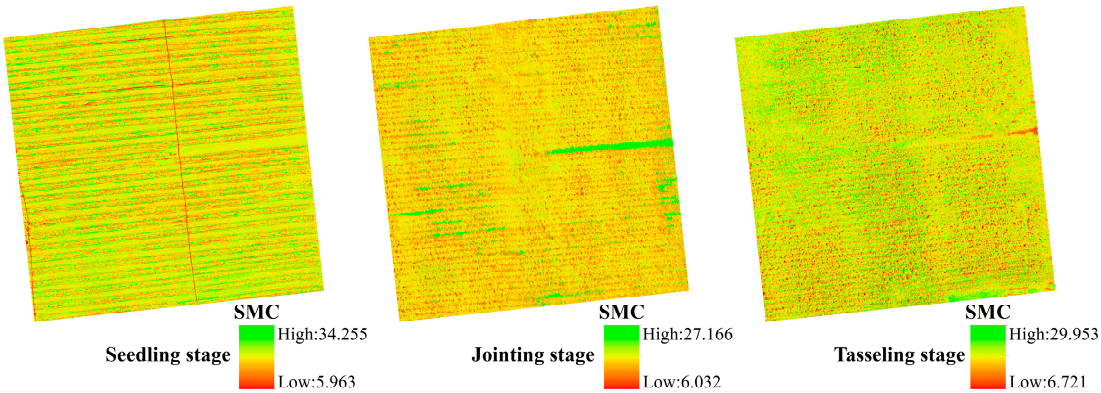

Figure 10. Inversion result graph.

4. Discussion

4.1. The Influence of Soil Background and Image Shadow on the Inversion Accuracy of SMC

SMC is a primary factor determining crop yield and quality. Real-time monitoring of its variation through UAV remote sensing is fundamental and crucial for achieving precise irrigation. Under stable conditions of light and temperature, SMC becomes a key factor affecting crop growth. Especially under water stress conditions, the crop's reflectance undergoes significant changes. However, existing studies show that due to the influence of multiple factors on UAV remote sensing platforms, the high-resolution multispectral imagery they capture is prone to interference from soil background and image shadows. When a single pixel contains reflectance information from multiple land cover types, the mixed spectra reduce the model's accuracy. These interferences weaken the spectral information of vegetation, reducing the accuracy of root zone SMC inversion [59,60]. Therefore, this study applies supervised classification to remove soil background and shadow areas from the imagery, reducing the spectral mixing effect, extracting only the plant reflection spectrum to create canopy vector files. By comparing the canopy spectral reflectance values before and after removing the soil background and image shadows, results indicate an improvement in canopy spectral reflectance values across all growth stages of silage corn. The most noticeable enhancement is observed in the near-infrared band, particularly during the seedling stage, which shows a more pronounced change in canopy spectral reflectance compared to the jointing and tasseling stages. Further analysis revealed that removing the soil background and image shadows improved the stability and robustness of the inversion model. This is consistent with the findings of Li Meixuan and Zhu Wenjing, who demonstrated an increase in R^2 to 0.723 by removing image shadows using the shadow index, thus improving nitrogen content inversion accuracy [61]. Zhu Wenjing used methods such as Otsu's method, threshold segmentation, and support vector machines for fine semantic segmentation of remote sensing images of wheat scab, increasing the R^2 of the validation set from 0.68 to 0.77, effectively enhancing the monitoring accuracy of wheat scab [62]. In this study, the improvement is particularly evident during the seedling stage, as the soil and maize seedlings are clearly distinguishable and easier to separate from the region of interest compared to the jointing and tasseling stages.

4.2. The Influence of Model on the Inversion Accuracy of SMC

This study employs three models—CNN [63], BPNN, and PLSR—to invert SMC. These models are based on different principles and algorithms, resulting in varying accuracy in

inversion. A CNN is a type of feedforward neural network with a convolutional structure, comprising an input layer, convolutional layers, pooling layers, fully connected layers, and an output layer [64,65]. It excels in handling spatial data, particularly in recognizing and analyzing images or spatial layouts. CNNs possess four main characteristics: local connectivity, weight sharing, pooling operations, and a multi-layered structure [66]. Their advantage lies in their ability to automatically learn features from data through multiple layers of nonlinear transformations, replacing manually designed features. The deep structure of CNNs endows them with strong representation and learning capabilities [67]. The BPNN is an effective model for parameter estimation, widely used in various prediction algorithms. However, it has a relatively slow convergence speed [68]. PLSR is a regression modeling method for multiple dependent variables (Y) against multiple independent variables (X). This algorithm extracts principal components from both Y and X while maximizing the correlation between the components derived from X and Y [69]. The study results indicate that the CNN model exhibited higher inversion accuracy, as the R^2 values for the modeling set were all around 0.9. Although the BPNN model's inversion accuracy was lower than that of the CNN and PLSR models, it still achieved good results on certain datasets, such as during the seedling stage. This suggests that different models have varying adaptability to the characteristics and structure of the input data. The comparison between the inverted SMC at the sampling points and the observed SMC is shown in Figure 11. Zhang et al. [70] utilized multispectral and thermal infrared remote sensing data collected throughout the entire growth stages of soybean and maize. By employing the random forest regression (RFR) model and combining indices to estimate SMC, their results indicated that multispectral remote sensing methods provided higher accuracy in SMC estimation compared to thermal infrared remote sensing. Seo et al. [71] collected multispectral and thermal infrared data to monitor SMC in large-scale potato fields. By comparing the SMC retrieval accuracy of CNN and deep neural networks (DNN), the results demonstrated that CNN exhibited superior performance in SMC estimation. Yin et al. [72] used alfalfa as the study object, acquiring RGB, multispectral, and thermal images to evaluate SMC using four regression models: PLSR, SVM, RF, and DNN. The results indicated that integrating multimodal data significantly improved the ability to estimate SMC, with the DNN model utilizing multimodal data achieving the best performance, yielding an R^2 of 0.72 and an RMSE of 4.98%. In this study, multispectral images of silage corn were acquired, and the removal of the soil background and image shadows, along with the selection of optimal variable combinations, significantly improved the accuracy of the SMC inversion model. CNN demonstrated superior accuracy and robustness in SMC inversion, followed by PLSR and BPNN. The specific performance of these models may vary depending on the study area, data type, and model parameters.

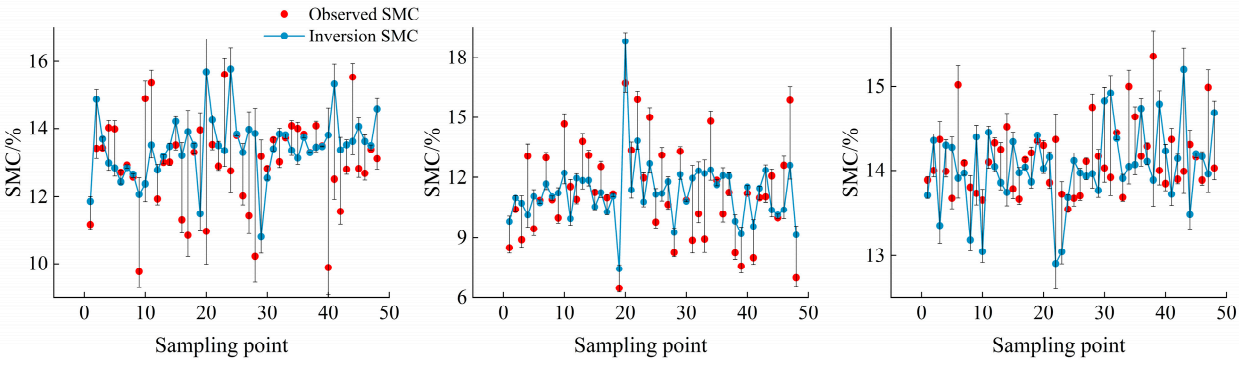

Figure 11. Comparison of inverted SMC and observed SMC at sampling point.

4.3. Uncertainty Analysis

The study on SMC inversion based on CNN, BPNN, and PLSR achieved satisfactory results, but some limitations remain. Although UAV technology is widely used in various fields, it is highly susceptible to weather conditions during flight. Thick cloud cover can significantly alter lighting conditions during the flight, resulting in unstable spectral data captured by the sensors. This leads to fluctuations in object reflectance, causing tonal shifts in multispectral images. Consequently, VIs used for SMC inversion (NDVI, GNDVI, etc.) are disturbed, as reflectance characteristics cannot maintain consistency, affecting the model's stability and predictive accuracy. In crop monitoring, such variations in lighting conditions influence the intensity of reflected light across different spectral bands, leading to color distortions that make inversion results inaccurate and compromise the analysis of critical indicators. Additionally, strong winds can destabilize the UAV, causing decreased spatial resolution, image quality, and positional accuracy. Furthermore, complex meteorological conditions may result in imaging data that are difficult to match with actual ground conditions.

To address these limitations, future research should focus on exploring real-time correction methods for spectral data instability caused by adverse meteorological conditions, as well as advanced image processing techniques to mitigate tonal shifts and spectral inconsistencies. For the instability caused by strong winds, future efforts should consider improving UAV stabilization technologies or integrating data from multiple sources, such as satellite imagery, to compensate for gaps resulting from UAV data limitations. These advancements would not only enhance the predictive capacity and accuracy of SMC inversion models, but also enable more informed decision-making in precision irrigation and agricultural environmental sustainability.

Agricultural data are sensitive to countries, due to political and ecological food security. However, these limitations are unfavorable for big data research. It is suggested that in the future work, data should be shared to construct an agricultural big data model and enhance the generalization of its interpretability under the premise of ensuring safety in a local range. This study focuses on the SMC retrieval of silage maize in the Hexi region, with methods that are particularly suitable for arid climates and crops with high water demand. The findings provide critical technical support for developing more generalizable precision irrigation systems and promoting sustainable agriculture in the future. For other crops or climatic regions, adjustments to model parameters would be necessary.

5. Conclusions

This paper aimed to investigate the impact of the soil background and image shadows on SMC inversion. First, supervised classification was used to remove soil background and image shadows. Then, Pearson correlation analysis was performed, showing a significant improvement in the correlation between independent variables (spectral indices) and the dependent variable (SMC). Finally, CNN, BPNN, and PLSR models were used to compare and analyze the inversion results at different growth stages, and their accuracy was evaluated.

(1) Due to the varying spectral characteristics of different bands, the VI constructed from canopy reflectance at different growth stages will differ. The correlation between NDVI1, GI, SIPI, and SMC was not significant before and after removing the soil background and image shadows. During the seedling and jointing stages, the correlation between NDVI1, GI, and SMC was near zero. Similarly, during the jointing and tasseling stages, the correlation between SIPI and SMC was near zero, indicating a nonlinear relationship or no apparent association between them.

(2) At each growth stage, removing the soil background and image shadows improved the accuracy of SMC inversion. In the CNN-based inversion model, the R^2 of the validation set increased by 20.33%, 0.92%, and 1.28% during the seedling, jointing, and tasseling stages, respectively, after removal. In the BPNN-based inversion model, the R^2 increased by 10.65%, 6.86%, and 17.20% during the seedling, jointing, and tasseling stages, respectively, after removal. In the PLSR-based inversion model, the R^2 increased by 2.87%, 31.55%, and 24.05% during the seedling, jointing, and tasseling stages, respectively, after removal. All three models showed the highest inversion accuracy during the seedling stage, with validation set R^2 values of 0.953, 0.821, and 0.895, respectively.

(3) The inversion accuracy of the three models before and after removing the soil background and image shadows followed the order seedling stage, tasseling stage, jointing stage. Removing the background improved the inversion accuracy at each growth stage numerically but did not alter the order of accuracy across growth stages.

Author Contributions: Writing—original draft preparation, Q.D.; project administration, J.Y. and G.L.; writing—review and editing, Q.D., Z.G. and W.W.; data curation, J.L. and H.L.; supervision, W.M.; software, Q.D., X.L. and K.C. All authors have read and agreed to the published version of the manuscript.

Funding: This work was sponsored in part by the Gansu Province 2024 Central Government-Guided Local Science and Technology Development Fund Project (24ZYQA023); the National Natural Science Foundation of China (42461060); the Gansu Provincial Key R&D Special Project on Ecological Civilization Construction (24YFFA059); the Gansu Province Department of Education Industry Support Program Project (2025CYZC-042); and the Gansu Province Financial Special Fund (GSCZZ 20160909).

Institutional Review Board Statement: Not applicable.

Data Availability Statement: The datasets generated and/or analyzed during the current study are not publicly available due limited availability of some data but are available from the corresponding author on reasonable request.

Acknowledgments: We sincerely thank the editor and reviewers for their time and effort in reviewing our work.

Conflicts of Interest: The authors declare that they have no known competing financial interests or personal relationships that could have appeared to influence the work reported in this paper.

References

1. Yang, X.; Pu, Y.W.; Weng, S.G.; Hou, M.; Wang, Z.H. Review of agricultural water-saving policies and measures in recent years—A case study of Jiangsu Province, China. *Water Sci. Technol. Water Supply* **2022**, *22*, 3951–3967. [CrossRef]
2. Ju, Q.Q.; Du, L.J.; Liu, C.S.; Jiang, S. Water resource management for irrigated agriculture in China: Problems and prospects. *Irrig. Drain.* **2023**, *72*, 854–863. [CrossRef]
3. Fertas, L.; Alouat, M.; Benmahamed, H. The Emergence of Irrigated Agriculture in Semi-Arid Zones in the Face of Climate Change and Urbanization in Peri-Urban Areas in Setif, Algeria. *Sustainability* **2024**, *16*, 1112. [CrossRef]
4. Liu, X.; Shi, L.J.; Qian, H.Y.; Sun, S.K.; Wu, P.T.; Zhao, X.N.; Engel, B.A.; Wang, Y.B. New problems of food security in Northwest China: A sustainability perspective. *Land Degrad. Dev.* **2020**, *31*, 975–989. [CrossRef]
5. Fan, Y.F.; He, L.Y.; Liu, Y.; Wang, S.F. Reallocating crop spatial pattern improves agricultural productivity and irrigation benefits without reducing yields. *Environ. Dev. Sustain.* **2023**, *25*, 14155–14176. [CrossRef]
6. Li, Y.; Xu, X.; Chen, Z.J.; Xiong, Y.W.; Huang, Q.Z.; Huang, G.H. A process simulation-based framework for resource, food, and ecology trade-off by optimizing irrigation and N management. *J. Hydrol.* **2023**, *617*, 129035. [CrossRef]
7. Zhao, X.; Tao, W.H.; Su, L.J.; Sun, Y.; Qu, Z.; Mu, W.Y.; Ma, C.K.; Shan, Y.Y. Spatio-Temporal Study on Irrigation Guarantee Capacity in the Northwest Arid Region of China. *Water* **2023**, *15*, 1396. [CrossRef]
8. Yin, Y.S.; Zhang, Y.N.; Duan, W.J.; Xu, K.; Yang, Z.H.; Shi, B.Y.; Yao, Z.Z.; Yin, C.B.; Dogot, T. Farmers' preferences for sustainable farmland construction—Insights from a discrete choice experiment in China. *Sustain. Prod. Consum.* **2024**, *48*, 235–247. [CrossRef]

9. Yang, M.M.; Zhu, Y.N.; Zhao, Y.; Li, C.M.; Zhang, Y.L.; Fan, Y.; Yang, W.J.; Kang, M.Y. Life cycle water and energy consumption and efficiency analysis of major crops in China. *J. Clean. Prod.* **2024**, *467*, 142899. [CrossRef]
10. Du, D.D.; Dong, B.; Zhang, R.; Cui, S.A.; Chen, G.R.; Du, F.F. Spatiotemporal dynamics of irrigated cropland water use efficiency and driving factors in northwest China's Hexi Corridor. *Ecol. Process.* **2024**, *13*, 72. [CrossRef]
11. Lan, S.; Zhang, Y.; Gao, T.Y.; Tong, F.H.; Tian, Z.Z.; Zhang, H.Y.; Li, M.Z.; Mustafa, N.S. UAV remote sensing monitoring of winter wheat tiller number based on vegetation pixel extraction and mixed-features selection. *Int. J. Appl. Earth Obs. Geoinf.* **2024**, *131*, 103940. [CrossRef]
12. Wang, J.H.; Ge, Y.; Heuvelink, G.B.M.; Zhou, C.H. Upscaling In Situ Soil Moisture Observations to Pixel Averages with Spatio-Temporal Geostatistics. *Remote Sens.* **2015**, *7*, 11372–11388. [CrossRef]
13. Zhu, W.X.; Rezaei, E.E.; Nouri, H.; Sun, Z.G.; Li, J.; Yu, D.Y.; Siebert, S. UAV-based indicators of crop growth are robust for distinct water and nutrient management but vary between crop development phases. *Field Crops Res.* **2022**, *284*, 108582. [CrossRef]
14. Resende, L.S.; Botrel, É.P.; Pozza, E.A.; Cássia Roteli, K.; Souza Andrade, O.C.; Martins Pereira, R.C. Effect of soil moisture, organic matter and fertilizer application on brown eye spot disease in coffee plantations. *Eur. J. Plant Pathol.* **2022**, *163*, 351–367. [CrossRef]
15. Guo, J.; Bai, Q.Y.; Guo, W.C.; Bu, Z.D.; Zhang, W.T. Soil moisture content estimation in winter wheat planting area for multi-source sensing data using CNNR. *Comput. Electron. Agric.* **2022**, *193*, 106670. [CrossRef]
16. Qu, T.T.; Li, Y.Y.; Zhao, Q.X.; Yin, Y.Z.; Wang, Y.Z.; Li, F.Z.; Zhang, W.P. Drone-Based Multispectral Remote Sensing Inversion for Typical Crop Soil Moisture under Dry Farming Conditions. *Agriculture* **2024**, *14*, 484. [CrossRef]
17. Cao, Z.Y.; Tang, L.Y.; Yuan, X.H.; Gand, Q. Surface topography modelling and ice flow velocity mapping of Dalk Glacier, East Antarctica: Application of UAV remote sensing. *Int. Arch. Photogramm. Remote Sens. Spat. Inf. Sci.* **2024**, *48*, 59–64. [CrossRef]
18. Wu, J.Y.; Wen, S.; Lan, Y.B.; Yin, X.C.; Zhang, J.T.; Ge, Y.F. Estimation of cotton canopy parameters based on unmanned aerial vehicle (UAV) oblique photography. *Plant Methods* **2022**, *18*, 129. [CrossRef] [PubMed]
19. Gago, J.; Douthe, C.; Coopman, R.E.; Gallego, P.P.; Ribas-Carbo, M.; Flexas, J.; Escalona, J.; Medrano, H. UAVs challenge to assess water stress for sustainable agriculture. *Agric. Water Manag.* **2015**, *153*, 9–19. [CrossRef]
20. Zhang, L.Y.; Zhang, H.H.; Niu, Y.X.; Han, W.T. Mapping maize water stress based on UAV multispectral remote sensing. *Remote Sens.* **2019**, *11*, 605. [CrossRef]
21. Barbedo, J.G.A. A Review on the Use of Unmanned Aerial Vehicles and Imaging Sensors for Monitoring and Assessing Plant Stresses. *Drones* **2019**, *3*, 40. [CrossRef]
22. Dharmaratne, P.P.; Salgadoe, A.S.A.; Rathnayake, W.M.U.K.; Weerasinghe, A.D.A.J.K.; Sirisena, D.N.; Wanninayaka, W.M.N. Remote Measurement of Nitrogen and Leaf Chlorophyll Concentration Using UAV-Based Multispectral Imagery from Rice Crop Field in Sri Lanka. *Sci. Data* **2023**, *980*, 641–654.
23. Castilho, D.; Tedesco, D.; Hernandez, C.; Madari, B.E.; Ciampitti, I. A global dataset for assessing nitrogen-related plant traits using drone imagery in major field crop species. *Sci. Data* **2024**, *11*, 585. [CrossRef] [PubMed]
24. Goffart, J.P.; Ben Abdallah, F.; Goffart, D.; Curnel, Y.; Planchon, V. Potato Crop Nitrogen Status Monitoring for Sustainable N Fertilisation Management: Last 15 Years and Future-Expected Developments with Reference Method and Use of Optical Sensors. *Potato Res.* **2023**, *66*, 1257–1303. [CrossRef]
25. Duangsuwan, S.; Teekapakvisit, C.; Maw, M.M. Development of soil moisture monitoring by using IoT and UAV-SC for smart farming application. *Adv. Sci. Technol. Eng. Syst. J.* **2020**, *5*, 381–387. [CrossRef]
26. Taghvaeian, S.; Chavez, J.L.; Hansen, N.C. Infrared Thermometry to Estimate Crop Water Stress Index and Water Use of Irrigated Maize in Northeastern Colorado. *Remote Sens.* **2012**, *4*, 3619–3637. [CrossRef]
27. Chakhar, A.; Hernández-López, D.; Ballesteros, R.; Moreno, M.A. Improvement of the Soil Moisture Retrieval Procedure Based on the Integration of UAV Photogrammetry and Satellite Remote Sensing Information. *Remote Sens.* **2021**, *13*, 4968. [CrossRef]
28. Shafian, S.; Maas, S.J. Index of Soil Moisture Using Raw Landsat Image Digital Count Data in Texas High Plains. *Remote Sens.* **2015**, *7*, 2352–2372. [CrossRef]
29. Liu, H.; Chen, J.Y.; Xiang, Y.Z.; Geng, H.S.; Yang, X.Z.; Yang, N.; Du, R.Q.; Wang, Y.; Zhang, Z.T.; Shi, L.S.; et al. Improving UAV hyperspectral monitoring accuracy of summer maize soil moisture content with an ensemble learning model fusing crop physiological spectral responses. *Eur. J. Agron.* **2024**, *160*, 127299. [CrossRef]
30. Qin, C.Y.; Zhou, J.P.; Xu, Y.; Duan, C.X.; Cui, C.; Zhang, H.Q. Using thermal infrared imaging to estimate soil moisture dynamics. *J. Irrig. Drain.* **2024**, *43*, 34.
31. Consoli, S.; Vanella, D. Mapping crop evapotranspiration by integrating vegetation indices into a soil water balance model. *Agric. Water Manag.* **2015**, *143*, 71–81. [CrossRef]
32. Wu, R.J.; Li, Q. Assessing the soil moisture drought index for agricultural drought monitoring based on green vegetation fraction retrieval methods. *Nat. Hazards* **2021**, *108*, 499–518. [CrossRef]

33. Almeida-Ñauñay, A.F.; Tarquis, A.M.; López-Herrera, J.; Pérez-Martín, E.; Pancorbo, J.L.; Raya-Sereno, M.D.; Quemada, M. Optimization of soil background removal to improve the prediction of wheat traits with UAV imagery. *Comput. Electron. Agric.* **2023**, *205*, 107559. [CrossRef]
34. Seo, M.G.; Shin, H.S.; Tsourdos, A. Soil Moisture Retrieval from Airborne Multispectral and Infrared Images using Convolutional Neural Network. *IFAC-Pap.* **2020**, *53*, 15852–15857. [CrossRef]
35. Singh, A.K.; Ganapathysubramanian, B.; Sarkar, S.; Singh, A. Deep Learning for Plant Stress Phenotyping: Trends and Future Perspectives. *Trends Plant Sci.* **2018**, *23*, 883–898. [CrossRef]
36. Yang, Z.H. Statistical Properties of the Maximum Likelihood Method of Phylogenetic Estimation and Comparison With Distance Matrix Methods. *Syst. Biol.* **1994**, *43*, 329–342. [CrossRef]
37. Goglio, L.; Rossetto, M. Comparison of fatigue data using the maximum likelihood method. *Eng. Fract. Mech.* **2004**, *71*, 725–736. [CrossRef]
38. Gao, Y.G.; Lin, Y.H.; Wen, X.L.; Jian, W.B.; Gong, Y.S. Vegetation information recognition in visible band based on UAV images. *Trans. Chin. Soc. Agric. Eng.* **2020**, *36*, 178–189.
39. Verrelst, J.; Schaepman, M.E.; Koetz, B.; Kneubühler, M. Angular sensitivity analysis of vegetation indices derived from CHRIS/PROBA data. *Remote Sens. Environ.* **2008**, *112*, 2341–2353. [CrossRef]
40. Rouse, J.W.; Haas, R.W.; Schell, J.A.; Deering, D.W. *Monitoring the Vernal Advancement and Retrogradation (Greenwave Effect) of Natural Vegetation*; Nasa/gsfct Type Final Report; NASA: Washington, DC, USA, 1974.
41. Sims, D.A.; Gamon, J.A. Relationships between leaf pigment content and spectral reflectance across a wide range of species, leaf structures and developmental stages. *Remote Sens. Environ.* **2002**, *81*, 337–354. [CrossRef]
42. Zarco-Tejada, P.J.; Berjón, A.; López-Lozano, R.; Miller, J.R.; Martín, P.; Cachorro, V.; González, M.R.; de Frutos, A. Assessing vineyard condition with hyperspectral indices: Leaf and canopy reflectance simulation in a row-structured discontinuous canopy. *Remote Sens. Environ.* **2005**, *99*, 271–287. [CrossRef]
43. Wang, F.M.; Huang, J.F.; Tang, Y.L.; Wang, X.Z. New Vegetation Index and Its Application in Estimating Leaf Area Index of Rice. *Rice Sci.* **2007**, *14*, 195–203. [CrossRef]
44. Penuelas, J.; Baret, F.; Filella, I. Semiempirical Indexes to Assess Carotenoids Chlorophyll-a Ratio from Leaf Spectral Reflectance. *Photosynthetica* **1995**, *31*, 221–230.
45. Xue, L.H.; Cao, W.X.; Luo, W.H.; Dai, T.B.; Zhu, Y. Monitoring Leaf Nitrogen Status in Rice with Canopy Spectral Reflectance. *Agron. J.* **2004**, *96*, 135–142. [CrossRef]
46. Mishra, S.; Mishra, D.R. Normalized difference chlorophyll index: A novel model for remote estimation of chlorophyll- a concentration in turbid productive waters. *Remote Sens. Environ.* **2011**, *117*, 394–406. [CrossRef]
47. Schneider, P.; Roberts, D.A.; Kyriakidis, P.C. A VARI-based relative greenness from MODIS data for computing the Fire Potential Index. *Remote Sens. Environ.* **2008**, *112*, 1151–1167. [CrossRef]
48. McFeeters, S.K. Using the Normalized Difference Water Index (NDWI) within a Geographic Information System to Detect Swimming Pools for Mosquito Abatement: A Practical Approach. *Remote Sens.* **2013**, *5*, 3544–3561. [CrossRef]
49. Kasim, N.; Sawut, R.; Shi, Q.; Maihemuti, B. Estimation of Soil Organic Matter Content Based on Optimized Spectral Index. *Nongye Jixie Xuebao/Trans. Chin. Soc. Agric. Mach.* **2018**, *49*, 11.
50. Janssens, O.; Walle, R.V.D.; Loccufier, M.; Hoecke, S.V. Deep Learning for Infrared Thermal Image Based Machine Health Monitoring. *IEEE/ASME Trans. Mechatron.* **2018**, *23*, 151–159. [CrossRef]
51. Speth, S.; Goncalves, A.; Rigault, B.; Suzuki, S.; Bouazizi, M.; Matsuo, Y.; Prendinger, H. Deep learning with RGB and thermal images onboard a drone for monitoring operations. *J. Field Robot.* **2022**, *39*, 840–868. [CrossRef]
52. He, Y.; Huo, T.B.; Gao, B.H.; Zhu, Q.; Jin, L.; Chen, J. Thaw Slump Susceptibility Mapping Based on Sample Optimization and Ensemble Learning Techniques in Qinghai-Tibet Railway Corridor. *IEEE J. Sel. Top. Appl. Earth Obs. Remote Sens.* **2024**, *17*, 5443–5459. [CrossRef]
53. Wang, W.N.; Yan, H.W.; Lu, X.M.; He, Y.; Liu, T.; Li, W.D.; Li, P.B.; Xu, F. Drainage pattern recognition method considering local basin shape based on graph neural network. *Int. J. Digit. Earth* **2023**, *16*, 593–619. [CrossRef]
54. Macbeth, C.; Dai, H.C. Effects of learning parameters on learning procedure and performance of a BPNN. *Neural Netw. Off. J. Int. Neural Netw. Soc.* **1997**, *10*, 1505–1521.
55. Kulkarn, A.H.; Rai, D.H.M.; Jahagirdar, D.K.A.; Upparamani, P.S. A Leaf Recognition Technique for Plant Classification Using RBPNN and Zernike Moments. *J. Comput. Mediat. Commun.* **2013**, *2*, 984–988.
56. Nawar, S.; Buddenbaum, H.; Hill, J.; Kozak, J. Modeling and Mapping of Soil Salinity with Reflectance Spectroscopy and Landsat Data Using Two Quantitative Methods (PLSR and MARS). *Remote Sens.* **2014**, *6*, 10813–10834. [CrossRef]
57. dos Santos, F.R.; de Oliveira, J.F.; Bona, E.; dos Santos, J.V.F.; Barboza, J.M.C.; Melquiades, F.L. EDXRF spectral data combined with PLSR to determine some soil fertility indicators. *Microchem. J.* **2020**, *152*, 104275. [CrossRef]
58. Tian, M.L.; Ge, X.Y.; Ding, J.L.; Wang, J.Z.; Zhang, Z.H. Coupled Machine Learning and Unmanned Aerial Vehicle Based Hyperspectral Data for Soil Moisture Content Estimation. *Laser Optoelectron. Prog.* **2020**, *57*, 232–241.

59. Yan, G.J.; Li, L.Y.; André Coy Mu, X.H.; Chen, S.B.; Xie, D.H.; Zhang, W.M.; Shen, Q.F.; Zhou, H.M. Improving the estimation of fractional vegetation cover from uav rgb imagery by colour unmixing. *ISPRS J. Photogramm. Remote Sens.* **2019**, *158*, 23–34. [CrossRef]
60. Aboutalebi, M.; Torres-Rua, A.F.; Kustas, W.P.; Nieto, H.; Coopmans, C.; McKee, M. Assessment of different methods for shadow detection in high-resolution optical imagery and evaluation of shadow impact on calculation of NDVI, and evapotranspiration. *Irrig. Sci.* **2019**, *37*, 407–429. [CrossRef]
61. Li, M.X.; Zhu, X.C.; Bai, X.Y.; Peng, Y.F.; Tian, Z.Y.; Jiang, Y.M. Remote Sensing Inversion of Nitrogen Content in Apple Canopy Based on Shadow Removal in UAV Multi-Spectral Remote Sensing Images. *Sci. Agric. Sin.* **2021**, *54*, 2084–2094.
62. Zhu, W.J.; Dai, S.Y.; Feng, Z.K.; Shao, C.F.; Duan, K.W.; Zhang, H.Y.; Wei, X.H. Optimizing wheat scab in remote sensing monitoring accuracy using interridge background elimination. *Trans. Chin. Soc. Agric. Eng.* **2024**, *40*, 219–229.
63. Chen, X.; Li, D.F.; Liu, M.Z.; Jia, J. CNN and Transformer Fusion for Remote Sensing Image Semantic Segmentation. *Remote Sens.* **2023**, *15*, 4455. [CrossRef]
64. Yan, X.F.; Ai, T.H.; Yang, M.; Yin, H.M. A graph convolutional neural network for classification of building patterns using spatial vector data. *ISPRS J. Photogramm. Remote Sens.* **2019**, *150*, 259–273. [CrossRef]
65. Selvaraju, R.R.; Cogswell, M.; Das, A.; Vedantam, R.; Parikh, D.; Batra, D. Grad-CAM: Visual Explanations from Deep Networks via Gradient-Based Localization. *Int. J. Comput. Vis.* **2020**, *128*, 336–359. [CrossRef]
66. Lecun, Y.; Bengio, Y.; Hinton, G. Deep learning. *Nature* **2015**, *521*, 436–444. [CrossRef] [PubMed]
67. Shin, H.C.; Roth, H.R.; Gao, M.C.; Lu, L.; Xu, Z.Y.; Nogues, I.; Yao, J.H.; Mollura, D.; Summers, R.M. Deep Convolutional Neural Networks for Computer-Aided Detection: CNN Architectures, Dataset Characteristics and Transfer Learning. *IEEE Trans. Med. Imaging* **2016**, *35*, 1285–1298. [CrossRef] [PubMed]
68. Liu, B.T. Review of swarm intelligence algorithm optimization of BP neural network. *Acad. J. Comput. Inf. Sci.* **2023**, *6*, 151–155.
69. Gad, M.; Saleh, A.H.; Hussein, H.; Elsayed, S.; Farouk, M. Water Quality Evaluation and Prediction Using Irrigation Indices, Artificial Neural Networks, and Partial Least Square Regression Models for the Nile River, Egypt. *Water* **2023**, *5*, 2244. [CrossRef]
70. Zhang, Y.L.; Yang, X.Y.; Tian, F. Study on Soil Moisture Status of Soybean and Corn across the Whole Growth Period Based on UAV Multimodal Remote Sensing. *Remote Sens.* **2024**, *16*, 3166. [CrossRef]
71. Seo, M.-G.; Shin, H.-S.; Tsourdos, A. Soil Moisture Retrieval Model Design with Multispectral and Infrared Images from Unmanned Aerial Vehicles Using Convolutional Neural Network. *Agronomy* **2021**, *11*, 398. [CrossRef]
72. Yin, L.B.; Yan, S.C.; Li, M.; Liu, W.Z.; Zhang, S.; Xie, X.Y.; Wang, X.X.; Wang, W.T.; Chang, S.H.; Hou, F.J. Enhancing soil moisture estimation in alfalfa root-zone using UAV-based multimodal remote sensing and deep learning. *Eur. J. Agron.* **2024**, *161*, 127366. [CrossRef]